

Frequency of extreme Sahelian storms tripled since 1982 in satellite observations

Christopher M. Taylor^{1,2}, Danijel Belušić^{1,3}, Françoise Guichard⁴, Douglas J. Parker⁵, Théo Vischel⁶, Olivier Bock⁷, Phil P. Harris^{1,2}, Serge Janicot⁸, Cornelia Klein¹ & Gérémy Panthou⁶

The hydrological cycle is expected to intensify under global warming¹, with studies reporting more frequent extreme rain events in many regions of the world^{2–4}, and predicting increases in future flood frequency⁵. Such early, predominantly mid-latitude observations are essential because of shortcomings within climate models in their depiction of convective rainfall^{6,7}. A globally important group of intense storms—mesoscale convective systems (MCSs)⁸—poses a particular challenge, because they organize dynamically on spatial scales that cannot be resolved by conventional climate models. Here, we use 35 years of satellite observations from the West African Sahel to reveal a persistent increase in the frequency of the most intense MCSs. Sahelian storms are some of the most powerful on the planet⁹, and rain gauges in this region have recorded a rise in ‘extreme’¹⁷ daily rainfall totals. We find that intense MCS frequency is only weakly related to the multidecadal recovery of Sahel annual rainfall, but is highly correlated with global land temperatures. Analysis of trends across Africa reveals that MCS intensification is limited to a narrow band south of the Sahara desert. During this period, wet-season Sahelian temperatures have not risen, ruling out the possibility that rainfall has intensified in response to locally warmer conditions. On the other hand, the meridional temperature gradient spanning the Sahel has increased in recent decades, consistent with anthropogenic forcing driving enhanced Saharan warming¹⁰. We argue that Saharan warming intensifies convection within Sahelian MCSs through increased wind shear and changes to the Saharan air layer. The meridional gradient is projected to strengthen throughout the twenty-first century, suggesting that the Sahel will experience particularly marked increases in extreme rain. The remarkably rapid intensification of Sahelian MCSs since the 1980s sheds new light on the response of organized tropical convection to global warming, and challenges conventional projections made by general circulation models.

The Clausius–Clapeyron relationship indicates that the water-holding capacity of the atmosphere increases by around 6–7% per degree Celsius. Assuming that humidity is the main driver of extreme rain, and that relative humidity remains constant, then changes in extreme rainfall should scale with temperature, according to this relationship⁷. Such scaling is largely reproduced by general circulation models (GCMs) in regions outside of the tropics, but is highly variable across models in the tropics¹¹. Rising temperatures may also intensify storm-scale dynamics, enhancing moisture inflow and the overall precipitation efficiency of rain events^{12,13}—features that are not well captured by GCMs; the importance of these processes for extreme rainfall probably depends on details of the local environment¹⁴. The difficulty in simulating these processes at multiple scales, coupled with

a general lack of long-term tropical observations, makes uncertainty in projections of extreme tropical rainfall particularly high⁷. These gaps in our fundamental knowledge of the climate system are of major societal importance for the populations who live in tropical land regions, not least in Africa, where the vast majority of agriculture is rain-fed, and the resilience of infrastructure to climatic change is low.

We focus here on data from the modern satellite era (1982–2016) from across the Sahel, the semi-arid region to the south of the Sahara. Sahel rainfall occurs during the active West African monsoon (WAM) months of June to September (JJAS), with approximately 90% of the rain being due to MCSs¹⁵. These travelling systems can extend many hundreds of kilometres, with lifetimes that may exceed one day¹⁶; but locally, rain typically falls within a couple of hours, associated with a line of convective cells at the front of the MCS. The Sahel experienced extreme decadal variability in rainfall during the twentieth century, with profound drought during the 1970s and 1980s following a very wet period in the 1950s and 1960s (ref. 17; Extended Data Fig. 1). Since the late 1990s, the five-year mean rainfall has recovered to more stable intermediate levels (Fig. 1a), but has retained strong interannual variability. Many researchers have emphasized the role of oceanic forcing on the decadal variability¹⁸, while recent studies have argued that the recovery is driven primarily by anthropogenic emissions of greenhouse gases¹⁹. At the same time, daily gauge totals¹⁷ (Fig. 1b) illustrate a marked rise in extreme rainfall (see Methods), above and beyond that observed during the very wet decades preceding the drought, and continuing to rise since the so-called recovery of the late 1990s.

We characterize properties of MCSs by using cloud-top temperatures from thermal infrared sensors onboard the geostationary Meteosat series of satellites. Although cloud-top temperature does not relate directly to rainfall, it is well suited to documenting the life cycle of MCSs^{15,16}; moreover, Meteosat provides a unique sub-daily time series of storms over more than three decades. For every Meteosat image, we define an MCS as a contiguous cold-cloud system exceeding 25,000 km². Using the widely adopted threshold for cold cloud of –40 °C, we find that more than 85% of extreme daily rain-gauge totals coincide with the passage of an MCS (Methods). However, the likelihood of extreme rain increases strongly with decreasing cloud-top temperature, as shown both from daily gauge accumulations, and from instantaneous space-borne radar estimates (Extended Data Fig. 2). Colder (hereafter, more ‘intense’) MCSs are also associated with increases in both the fractional area of convective rain and the westward propagation speed (see Methods).

The time series of MCS frequency at –40 °C is highly correlated with seasonal mean rainfall (Table 1), consistent with previous studies¹⁵. In Fig. 1c, d, we show trends in MCS frequency sampled at 1800 UTC—a

¹Centre for Ecology and Hydrology, Wallingford OX10 8BB, UK. ²National Centre for Earth Observation, Wallingford OX10 8BB, UK. ³Swedish Meteorological and Hydrological Institute, Norrköping SE-601 76, Sweden. ⁴Centre National de Recherches Météorologiques (CNRM), UMR 3589, Centre National de la Recherche Scientifique (CNRS) & Météo-France, 31057 Toulouse Cedex, France.

⁵School of Earth and Environment, University of Leeds, Leeds LS2 9JT, UK. ⁶Univ. Grenoble Alpes, l’Institut de Recherche pour le Développement (IRD), CNRS, Institute of Engineering Univ. Grenoble Alpes (G-INP), Institut des Géosciences de l’Environnement (IGE), F-38000 Grenoble, France. ⁷Institut national de l’information géographique et forestière (IGN) Laboratoire de Recherche en Géodésie (LAREG), Université Paris Diderot, Sorbonne Paris Cité, 75205 Paris, France. ⁸UMR7159, Laboratoire d’Océanographie et du Climat: Expérimentations et Approches Numérique (LOCEAN), Sorbonne Universités, l’Université Pierre et Marie Curie (UPMC)-CNRS-l’Institut de Recherche pour le Développement (IRD)-Muséum National d’Histoire Naturelle (MNHN), 75252 Paris, France.

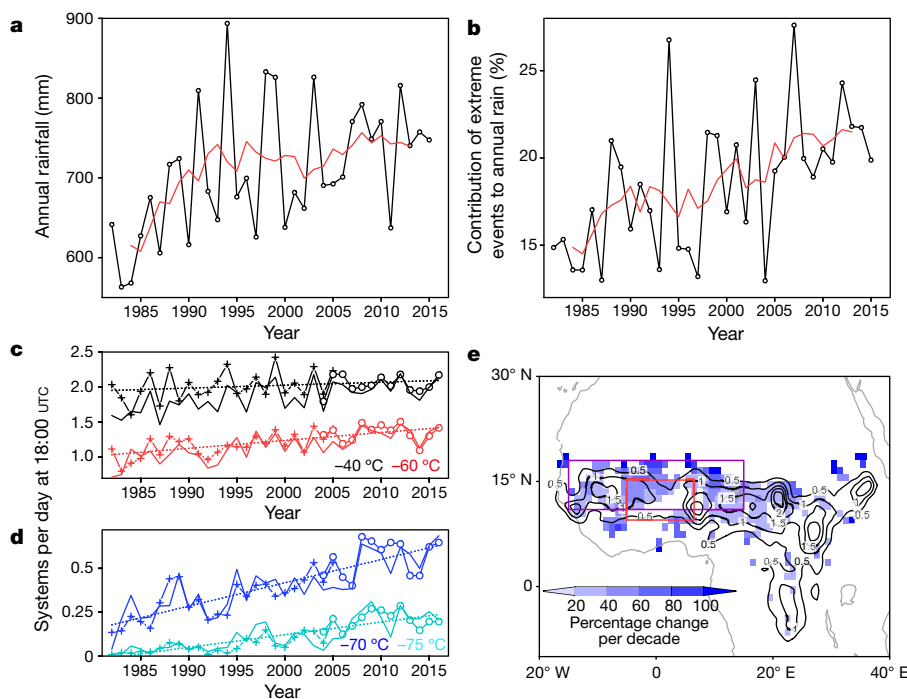


Figure 1 | Trends in MCS and rainfall characteristics across the Sahel. **a, b,** Annual rainfall (**a**), and contribution of extreme events to annual rainfall (**b**), as measured by a daily rain-gauge network. Red lines indicate five-year running means. **c, d,** Regional MCS frequency at 1800 UTC at different temperature thresholds, derived directly from measurements onboard the Meteosat First Generation (MFG; + symbols) and Meteosat Second Generation (MSG; O symbols) geostationary satellites. The cross-calibrated GridSat version of these data is shown as a solid line. Dotted lines denote trends. **e,** Significant trends ($P < 0.05$) in MCS cloud cover at 1800 UTC (using a temperature threshold of -70°C). Trends are expressed as a percentage change per decade, relative to the 35-year mean (contours). The red and purple rectangles denote the domains used in **a, b** and **c, d**, respectively.

time of day when, typically, MCSs have reached their mature phase¹⁶. Interestingly, as the temperature threshold is reduced, the time series start to resemble strong linear trends. At a threshold of -70°C , the trend at 1800 UTC amounts to a remarkable 3.5-fold increase over 35 years, or a 3.7-fold increase over 35 years when averaged over 24 hours (Extended Data Fig. 3). The rise in intense MCS frequency is driven by a downward trend in MCS mean temperature (0.78°C per decade for -40°C systems; Extended Data Fig. 4). Intense MCS frequency is highly correlated with global land temperature (Table 1), yielding sensitivities of +99% (at -70°C) and +200% (at -75°C) per degree of global land temperature. Notably, the rise in frequency of intense MCSs has continued since the recovery of the late 1990s, in the absence of a trend in annual rainfall; that is, the intensification signal emerges above the strong decadal variability of total rainfall in this region¹⁷.

The spatial extent of the trend in intense African MCSs is restricted in JJAS to a narrow Sahelian belt (Fig. 1e). Trends over the full annual cycle (Extended Data Fig. 5) show that the signal extends down to the Guinea Coast during the boreal spring, but there is no evidence of similarly extensive trends elsewhere in Africa, including the Congo Basin, another global hotspot of intense storms⁹. Analysis of the diurnal cycle (Extended Data Fig. 3) indicates that positive trends in MCS frequency at -70°C are significant ($P < 0.005$) at all times of day, and are in phase with the typical MCS life cycle of afternoon initiation, peak frequency in the evening, and decay during the morning hours. Positive trends in the size of the largest MCSs are modest for most times of day and temperature thresholds, and become significant ($P < 0.01$) during the evening for the most intense systems. At all times of day, however, the trend in total coverage of the coldest systems is dominated by changes in

frequency, not area. The diurnal phase of these trends implies that they are driven by more intense convection in late afternoon and evening, in turn creating larger, longer-lived systems overnight.

Potential drivers of this rapid regional intensification of MCSs include mineral aerosol concentrations and vegetation cover, although neither exhibits a well defined trend that includes the past ten years^{20,21}. Instead, the high correlation with global temperature suggests a response to atmospheric warming. Observational and reanalysis data sets agree that near-surface Sahelian temperature trends (during JJAS) over this period have been small or negative (Fig. 2), presumably a direct response to increased rainfall, cloud, and surface evaporative cooling following the multidecadal drought. The intensification of MCSs cannot therefore be a simple response to rising local temperature. However, there is a consensus across data sets that the Sahara has been warming more rapidly than the rest of Africa^{19,22}, although spatial patterns differ, linked to the sparse and temporally varying measurement network. Saharan warming has therefore driven an increase in the meridional temperature gradient. While most historical GCM simulations from the fifth coupled model intercomparison project (CMIP5) do not capture the Sahelian drought recovery, the trend in the simulated temperature gradient is a robust response across the ensemble to greenhouse gas emissions, and is projected to continue to intensify throughout the twenty-first century (Fig. 2e).

We now consider the role of atmospheric variables that are known to influence MCS properties, through correlations with MCS intensity at both event (Extended Data Fig. 7) and annual (Extended Data Fig. 8) timescales (see Methods). First, it has been known for several decades that wind shear organizes convection into long-lived and large-scale systems²³. We find significant correlations ($P < 0.005$) between pre-MCS zonal wind shear and MCS intensity, consistent with recent theory that shear dominates the intensity of MCSs²⁴. The intensification trend is also correlated with increasing low-level westerlies, and with the African Easterly Jet. Second, mid-level dry air intensifies Sahelian MCSs (via enhanced evaporative downdrafts)^{25,26}, and we find significant correlations between MCS intensity and relative humidity at 700 hPa on both timescales.

Another important factor for convection is low-level moisture; a dry planetary boundary layer (PBL) tends to suppress the development of MCSs through a lack of convective available potential energy (CAPE). Interestingly, though, we find no significant correlation between MCS

Table 1 | Linear correlation statistics for 24-hour mean MCS frequencies at different temperature thresholds

Temperature threshold ($^{\circ}\text{C}$)	Correlation coefficient (P value)		
	Linear trend	Sahel rain	Global temperature
-40	0.41 (0.007)	0.88 (<0.00001)	0.37 (0.0162)
-60	0.77 (<0.00001)	0.83 (0.00015)	0.77 (<0.00001)
-70	0.87 (<0.00001)	0.65 (0.00002)	0.82 (<0.00001)
-75	0.88 (<0.00001)	0.56 (0.00036)	0.80 (<0.00001)

Global land mean temperatures (shown in Extended Fig. 1c) are computed from JJAS averages.

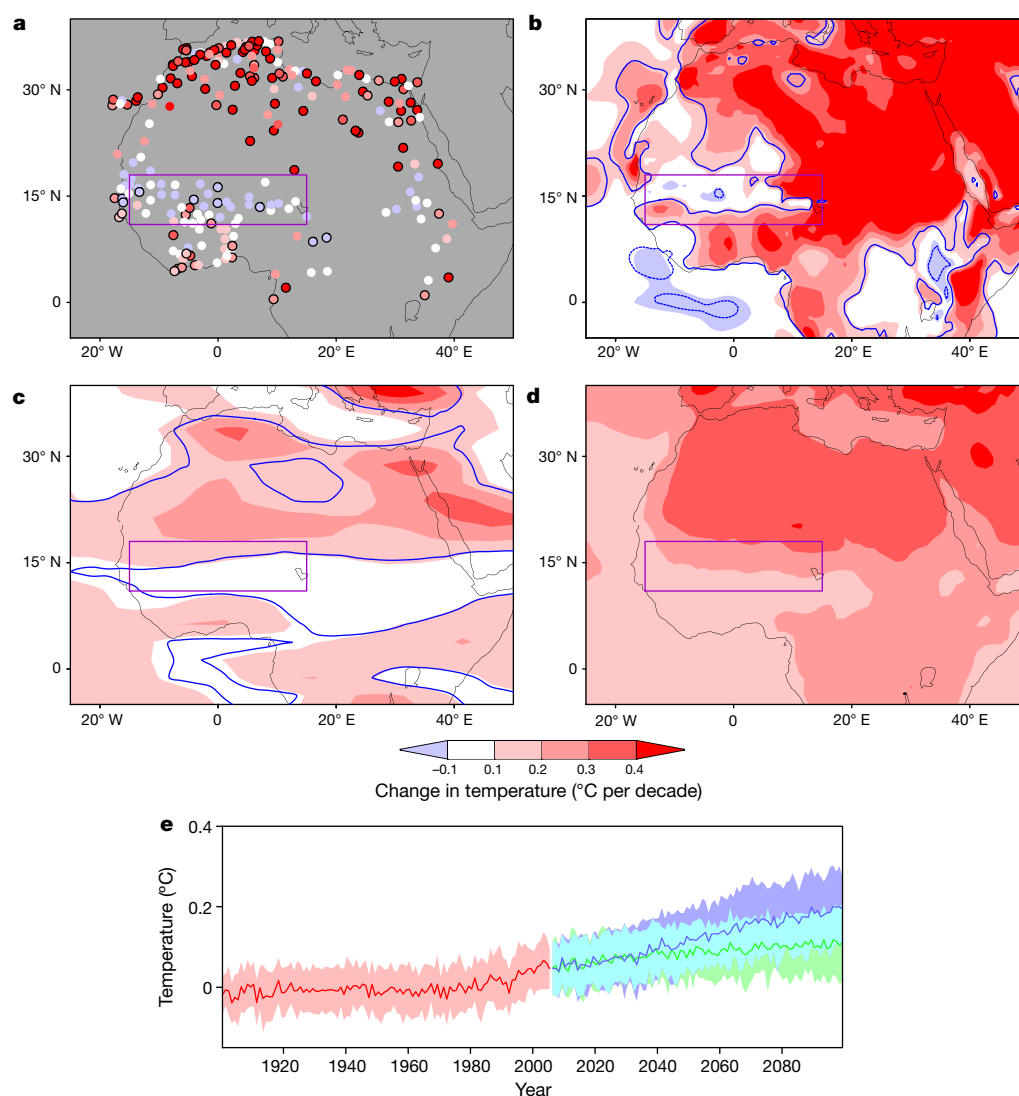


Figure 2 | Temperature trends (for June to September) in observations and models. a–d, Trends (shown as change in temperature (°C) per decade) are derived from: **a**, synoptic stations; **b**, ERA-Interim reanalysis; **c**, lower tropospheric temperature derived from microwave sounding data; and **d**, CMIP5-ensemble-based mean for historical runs. **e**, The meridional temperature gradient (20° N minus 10° N; average over 15° W to 15° E) from the CMIP5 historical (red), RCP4.5 (green) and RCP8.5 (purple) ensembles (relative to 1961–1990; shading denotes the standard deviation for each ensemble). Temperatures were taken at a height of 2 metres, except in panel **c**, which samples the lower troposphere. Trends are computed for the period 1982–2015, except in panel **d**, which covers 1976–2005. Significant positive and negative trends ($P < 0.05$) are denoted by solid black circles (**a**), or lie within blue contours (**b**, **c**). The rectangles mark the region of the Sahel that was used for computing MCS statistics.

intensity and low-level specific humidity at either the event or the annual timescale, a factor we return to below. We do however find event-scale relationships between MCS intensity and both higher temperatures and weaker southerly winds at low and mid-levels. These variables are not independent, and, in particular, co-vary with the phase of African easterly waves (AEWs), the dominant synoptic feature in the region. With the exception of mid-level temperatures, however, their respective correlations with MCS intensity at event and annual scales differ in sign (see Methods), suggesting that trends in these variables cannot explain intensification. Mid-level warming suppresses the early development of small convective clouds, therefore allowing the accumulation of more CAPE and enabling more intense systems to develop once they have been triggered. As regards synoptic variability, AEWs modulate MCS frequency, and climate projections suggest that there will be more intense AEWs by 2100 under greenhouse forcing²⁷, driven by increasing baroclinicity. We are unaware of previous work showing observed multidecadal trends in AEWs, but we note the strong correlation (Extended Data Fig. 8f) between MCS intensity and enhanced low-level synoptic variability to the north of the Sahel in the ERA-Interim reanalysis, suggestive of a role of increasing AEWs in MCS intensification. Finally, widespread tropopause cooling has been reported as a response to greenhouse gas emissions. Because upper-tropospheric observations and reanalyses are unreliable in this data-sparse region²⁸, one cannot rule out a role for this process in MCS intensification.

The observed increase in extreme precipitation inferred from MCS properties has not been accompanied by trends in precipitable water

or specific humidity (Extended Data Fig. 8). Composite time series of precipitable-water measurements (Methods) depict a rapid moistening in the three to four hours ahead of an MCS (Fig. 3), owing to moisture flux convergence. However, although MCS intensity is highly correlated with precipitable water at the time of passage, there is no significant signal with precipitable water when measured six hours ahead. This is an example of MCS-scale dynamic processes that lead to rainfall intensification beyond the limits of the local thermodynamic profile; the same dynamic processes can explain our observed multidecadal trends. We conclude that the most likely drivers of Sahelian MCS intensification are enhanced shear and mid-level drying, consistent with well established mechanisms. In addition, mid-level warming and enhanced synoptic variability could have played a role. These mechanisms are all directly linked to a warming Sahara; baroclinicity enhances shear and drives AEWs, while the mid-level Saharan air layer (SAL) in the Sahel is adiabatically connected to the Saharan PBL²⁹.

Assuming that the present-day physical relationships linking Saharan warming with Sahelian MCS intensity hold in the future, projections of enhanced baroclinicity suggest that extreme daily rainfall totals will continue to rise rapidly, regardless of (highly uncertain) seasonal mean rainfall projections. We found that existing GCMs cannot reproduce the observed rate or spatial pattern of extreme rainfall intensification, presumably in part because they cannot capture key physical processes responsible for organized convection. For example, convective parameterizations are insensitive to shear and exhibit a rather weak dependence on moisture in the free troposphere³⁰.

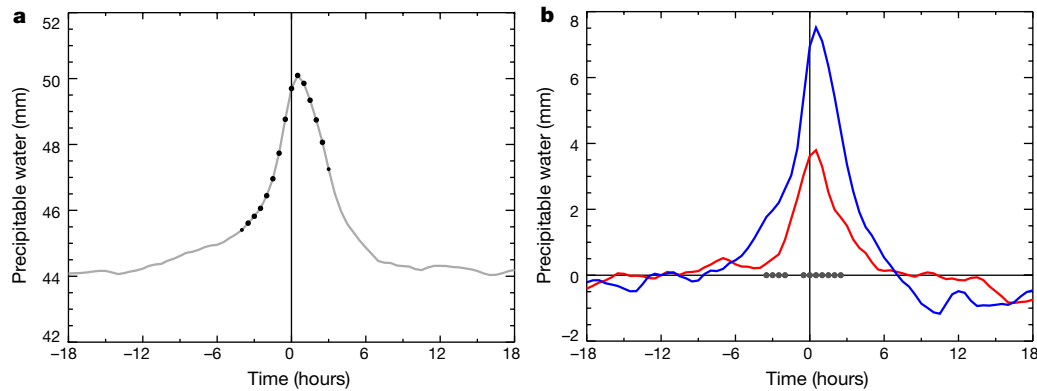


Figure 3 | Evolution of observed precipitable water, measured at GPS stations. **a**, Composite mean precipitable water (mm) associated with the passage (at 0 h) of 496 Sahelian MCSs. Small (or large) circles denote times when precipitable water correlates significantly with MCS intensity

New, high-resolution (less than 5 km) convection-permitting simulations are needed to explore how MCSs respond to enhanced Saharan warming. As the world continues to warm, we may find rapid MCS intensification signals emerging in other regions of the world, where the Clausius–Clapeyron relationship (and indeed present GCM extreme rain projections) are of little value. In West Africa, the impact of recent severe flash floods provides an indication of the challenges ahead for urban planners. For example, in 2009, a downpour of 263 mm over several hours forced 150,000 residents of Ouagadougou (in Burkina Faso) to leave their homes. Further intensification of MCSs will reduce flood return times, and increase the risk of disease outbreaks due to poor sanitation systems. Thus reliable information on the changing hydroclimate urgently needs to be incorporated into plans for West Africa's rapidly expanding cities.

Online Content Methods, along with any additional Extended Data display items and Source Data, are available in the online version of the paper; references unique to these sections appear only in the online paper.

Received 6 October 2016; accepted 13 March 2017.

- Allen, M. R. & Ingram, W. J. Constraints on future changes in climate and the hydrologic cycle. *Nature* **419**, 224–232 (2002).
- Westra, S. *et al.* Future changes to the intensity and frequency of short-duration extreme rainfall. *Rev. Geophys.* **52**, 522–555 (2014).
- Min, S.-K., Zhang, X., Zwiers, F. W. & Hegerl, G. C. Human contribution to more-intense precipitation extremes. *Nature* **470**, 378–381 (2011).
- Donat, M. G., Lowry, A. L., Alexander, L. V., O'Gorman, P. A. & Maher, N. More extreme precipitation in the world's dry and wet regions. *Nat. Clim. Chang.* **6**, 508–513 (2016).
- Kundzewicz, Z. W. *et al.* Flood risk and climate change: global and regional perspectives. *Hydrol. Sci. J.* **59**, 1–28 (2014).
- Kendon, E. J. *et al.* Heavier summer downpours with climate change revealed by weather forecast resolution model. *Nat. Clim. Chang.* **4**, 570–576 (2014).
- O'Gorman, P. A. Precipitation extremes under climate change. *Curr. Clim. Change Rep.* **1**, 49–59 (2015).
- Houze, R. A. Mesoscale convective systems. *Rev. Geophys.* **42**, RG4003 (2004).
- Zipser, E. J., Liu, C., Cecil, D. J., Nesbitt, S. W. & Yorty, D. P. Where are the most intense thunderstorms on Earth? *Bull. Am. Meteorol. Soc.* **87**, 1057–1071 (2006).
- Biasutti, M., Held, I. M., Sobel, A. H. & Giannini, A. SST forcings and Sahel rainfall variability in simulations of the twentieth and twenty-first centuries. *J. Clim.* **21**, 3471–3486 (2008).
- O'Gorman, P. A. Sensitivity of tropical precipitation extremes to climate change. *Nat. Geosci.* **5**, 697–700 (2012).
- Singleton, A. & Toumi, R. Super-Clausius–Clapeyron scaling of rainfall in a model squall line. *Q. J. R. Meteorol. Soc.* **139**, 334–339 (2013).
- Berg, P., Moseley, C. & Haerter, J. O. Strong increase in convective precipitation in response to higher temperatures. *Nat. Geosci.* <http://dx.doi.org/10.1038/ngeo1731> (2013).
- Muller, C. Impact of convective organization on the response of tropical precipitation extremes to warming. *J. Clim.* **26**, 5028–5043 (2013).
- Mathon, V., Laurent, H. & Lebel, T. Mesoscale convective system rainfall in the Sahel. *J. Appl. Meteorol.* **41**, 1081–1092 (2002).
- Futyan, J. M. & Del Genio, A. D. Deep convective system evolution over Africa and the tropical Atlantic. *J. Clim.* **20**, 5041–5060 (2007).

at $P < 0.05$ (or $P < 0.01$). **b**, Evolution of precipitable-water anomalies sampled from events in the lower (blue) and upper (red) quartiles of MCS temperature. Circles denote times when the two time series differ significantly ($P < 0.05$).

- Panthou, G., Vischel, T. & Lebel, T. Recent trends in the regime of extreme rainfall in the Central Sahel. *Int. J. Climatol.* **34**, 3998–4006 (2014).
- Giannini, A., Saravanan, R. & Chang, P. Oceanic forcing of Sahel rainfall on interannual to interdecadal time scales. *Science* **302**, 1027–1030 (2003).
- Dong, B. & Sutton, R. Dominant role of greenhouse-gas forcing in the recovery of Sahel rainfall. *Nat. Clim. Chang.* **5**, 757–760 (2015).
- Evan, A. T., Flamant, C., Gaetani, M. & Guichard, F. The past, present and future of African dust. *Nature* **531**, 493–495 (2016).
- Dardel, C. *et al.* Re-greening Sahel: 30 years of remote sensing data and field observations (Mali, Niger). *Remote Sens. Environ.* **140**, 350–364 (2014).
- Cook, K. H. & Vizi, E. K. Detection and analysis of an amplified warming of the Sahara Desert. *J. Clim.* **28**, 6560–6580 (2015).
- Rotunno, R., Klemm, J. B. & Weisman, M. L. A theory for strong, long-lived squall lines. *J. Atmos. Sci.* **45**, 463–485 (1988).
- Alfaro, D. A. Low-tropospheric shear in the structure of squall lines: impacts on latent heating under layer-lifting ascent. *J. Atmos. Sci.* **74**, 229–248 (2017).
- Barnes, G. M. & Sieckman, K. The environment of fast- and slow-moving tropical mesoscale convective cloud lines. *Mon. Weath. Rev.* **112**, 1782–1794 (1984).
- Roca, R., Lafore, J.-P., Piriou, C. & Redelsperger, J.-L. Extratropical dry-air intrusions into the West African monsoon midtroposphere: an important factor for the convective activity over the Sahel. *J. Atmos. Sci.* **62**, 390–407 (2005).
- Skinner, C. B. & Diffenbaugh, N. S. Projected changes in African easterly wave intensity and track in response to greenhouse forcing. *Proc. Natl Acad. Sci. USA* **111**, 6882–6887 (2014).
- Seidel, D. J. & Randel, W. J. Variability and trends in the global tropopause estimated from radiosonde data. *J. Geophys. Res.* **111**, D21101 (2006).
- Parker, D. J., Thorncroft, C. D., Burton, R. R. & Diongue-Niang, A. Analysis of the African easterly jet, using aircraft observations from the JET2000 experiment. *Q. J. R. Meteorol. Soc.* **131**, 1461–1482 (2005).
- Del Genio, A. D. Representing the sensitivity of convective cloud systems to tropospheric humidity in general circulation models. *Surv. Geophys.* **33**, 637–656 (2012).

Acknowledgements The research leading to these results received funding from the UK's National Environment Research Council (NERC)/Department for International Development (DFID) Future Climate For Africa programme, under the AMMA-2050 project (grant numbers NE/M020428/1, NE/M019969/1, NE/M019950/1, NE/M020126/1 and NE/M019934/1). D.J.P. is supported by a Royal Society Wolfson Research Merit Award. We thank K. Knapp, J. Marsham and D. Kniveton for helpful comments; J. Griffin for assistance in preparing the figures; the providers of key data sets used here (Eumetsat; the US National Oceanic and Atmospheric Administration (NOAA); NASA; the European Centre for Medium-Range Weather Forecasts (ECMWF); the meteorological services of Mali, Burkina Faso, Niger and Benin; the World Climate Research Programme's Working Group on Coupled Modelling); and the centres that provided modelling data.

Author Contributions This study was conceived by C.M.T. and T.V.; C.M.T., D.B., F.G., D.J.P., T.V. and S.J. designed the research; C.M.T., D.B., F.G., P.P.H., C.K. and G.P. analysed the data; and O.B. provided expertise on the GPS analysis. C.M.T. wrote the manuscript, which all authors commented on.

Author Information Reprints and permissions information is available at www.nature.com/reprints. The authors declare no competing financial interests. Readers are welcome to comment on the online version of the paper. Publisher's note: Springer Nature remains neutral with regard to jurisdictional claims in published maps and institutional affiliations. Correspondence and requests for materials should be addressed to C.M.T. (cmt@ceh.ac.uk).

Reviewer Information *Nature* thanks C. Liu and the other anonymous reviewer(s) for their contribution to the peer review of this work.

METHODS

Cloud-top temperature data. The principal data used here are cloud-top temperatures—detected from the series of geostationary Meteosat satellites—which we use to quantify the evolution of MCS characteristics. As the satellites are located at 0° E, 0° N, these data provide excellent coverage of tropical Africa. Archived data (downloaded from Eumetsat, <http://www.eumetsat.int>) are available from 1982 to the present. We use measurements from nine satellites in the series, from Meteosat-2 (1982) to Meteosat-10 (2016). Meteosat First Generation (MFG; ending in July 2006) satellites carried the Meteosat visible and infrared imager, providing thermal infrared data (10.5–12.5 μm) every 30 minutes at a resolution of about 4.5 km at the equator. From 2004 onwards, this was superseded by the spinning enhanced visible and infrared imager on Meteosat Second Generation (MSG) platforms. This provides higher spatial (about 3 km) and temporal (15 minute) resolution, and additional channels: here we use MSG channel 9 (centred at 10.8 μm). We used the coefficients provided by Eumetsat to convert the data from counts to brightness temperatures (<http://www.eumetsat.int/website/home/Data/Products/Calibration/index.html>). Up to May 2000, a vicarious calibration technique was adopted using a sea-surface target. The top-of-atmosphere radiance was estimated using data from the National Centers for Environmental Prediction analysis. Since then, the Meteosat sensors have benefited from an onboard black-body calibration mechanism. To minimize the impact of the change in pixel size from MFG to MSG, we degraded the images to an approximately common resolution of 9 km (2×2 MFG pixels, 3×3 MSG pixels), and only used half-hourly MSG data.

For a given temperature threshold, we define MCSs in each image from contiguous cold-cloud systems that exceed an areal threshold of 25,000 km². We chose this areal threshold on the basis of comparison of cold-cloud structures with daily rain-gauge measurements (see below). Four temperature thresholds are used: -40°C , -60°C , -70°C and -75°C . We define a geographical domain spanning the Western and Central Sahel (15°W to 15°E , 11°N to 18°N ; plotted in Fig. 1e), over which we computed MCS properties for every available half-hourly image for the monsoon months of June to September. Each MCS centred within the domain was counted, and Fig. 1c, d presents these data (for 1800 UTC) as the sum of MCSs divided by the number of images available in that season. Trends in MCS frequency at other times of day are shown in Extended Data Fig. 3, and correlations of the 35-year time series in Table 1 are computed using average MCS frequencies over all 48 images within a day. We found that, on average, the daily minimum in the minimum temperature for each MCS at a threshold of -40°C occurred at 1700 UTC, denoting the end of the vertical development phase¹⁶ and the onset of the mature phase, marked by horizontal growth. The likelihood of observing intense rainfall rates in spaceborne precipitation radar data (see below) was maximized during the period 1800–2100 UTC, associated with mature MCSs. When assessing spatial variations in trends (Fig. 1e), for each image we computed the fractional coverage of pixels within an MCS at 1° spatial resolution. Throughout, trends in MCS frequency are expressed as a percentage relative to the mean.

We explored the sensitivity of MCS properties to different temperature thresholds using independent observations. This was to verify that lower temperature thresholds are on average representative of more intense MCSs. The westward propagation speed was computed for every MCS in consecutive half-hourly images by identifying the length scale at which the maximum spatial correlation of brightness temperatures occurred. This revealed a clear sensitivity of propagation speed, with mean values of 12.0 m s⁻¹, 14.4 m s⁻¹, 16.6 m s⁻¹ and 18.3 m s⁻¹ for MCS temperature thresholds of -40°C , -60°C , -70°C , and -75°C respectively. We also computed the likelihood of MCS passage over an individual rain gauge on a day that received intense rainfall, and how this likelihood varied with areal threshold and cloud-top temperature (Extended Data Fig. 2a, b). Using 19 Sahelian stations at latitudes between 13.0°N and 15.3°N , the minimum cloud-top temperature and maximum contiguous cloud area affecting pixels within 7.5 km of the gauge were recorded for each day on which rain exceeded 10 mm. We examined those data in which rain exceeded an intense rainfall threshold, on the basis of the average of individual station thresholds (see below), which for this limited range of latitudes gave a rainfall amount of 38 mm. While a small fraction of these cases (12%) registered no local cold cloud (with a temperature of -40°C or less) over 24 hours, overall the likelihood of intense rain coinciding with an MCS at a temperature threshold of -40°C and an areal threshold of 25,000 km² was 85.5% (rising to 96% if no cold-cloud cases were excluded; Extended Data Fig. 2a). Considering only those cases in which this areal threshold was satisfied, Extended Data Fig. 2b illustrates the expected strong sensitivity of daily rainfall to minimum pixel temperature. We found that 88% of all extreme events are associated with minimum temperatures of -70°C or lower, and the coldest 20% of cloud-top temperatures account for nearly one-third of the extreme measurements.

Finally, we overlaid the MCS data set (with a threshold of -40°C) in space and time, with precipitation radar data from 1,640 overpasses from the Tropical

Rainfall Measurement Mission (TRMM) over the period 2004 to 2013. Radar-based estimates of surface rainfall rate and the type of rain (convective or stratiform) are provided within the TRMM2A25 product (available from <http://disc.sci.gsfc.nasa.gov/precipitation>). Extended Data Fig. 2c clearly illustrates how the probability of extreme rainfall rate (defined here as the 98th percentile of all TRMM observations, equivalent to 30 mm rainfall per hour) within an MCS rises with decreasing MCS temperature. We found that 38% of extreme events are associated with the coldest 20% of MCSs. We also examined the rainfall type for all TRMM pixels with non-zero rain within each MCS. We found that the fraction of rainy pixels that were convective rose from 20% to 30% as the mean MCS temperature decreased from -40°C to -70°C .

The Meteosat series was designed for the operational meteorological community rather than for long-term monitoring. To address the needs of climate research, recent efforts have been made to homogenize these data, alongside other geostationary series, resulting in the global GridSat climate data record³¹. This data set built on the work of the International Satellite Cloud Climatology Project (ISCCP), which provided an absolute calibration of geostationary measurements through the use of advanced very high resolution radiometer data onboard polar-orbiting satellites. The GridSat product benefits from a second intercalibration with observations from the high-resolution infrared radiation sounder. This additional step allows for the detection and correction of biases in the ISCCP product^{31,32}. The estimated calibration uncertainty in this product is less than 0.1 $^\circ\text{C}$ per decade. The data (available at www.ncdc.noaa.gov/gridsat) are corrected for view angle and parallax and stored on a 0.07° grid every 3 hours. We used GridSat data spanning the period January 1982 to September 2016.

We focus here on the frequency of MCSs at different temperature thresholds—a measure that is rather insensitive to biases and drifts in brightness temperature when using the uncorrected Eumetsat data set. This important aspect is illustrated in Fig. 1c, d, which show a high degree of consistency in MCS frequencies obtained from Meteosat-7 (from the MFG series) and Meteosat-8 (the first MSG satellite) during the MFG/MSG overlap period of 2004–2005. Crucially, the trends in MCS frequency based on the Eumetsat data are reproduced by the GridSat record. Moreover, time series of mean MCS temperature (at -40°C) exhibit a clear downward trend over the 35 years (Extended Data Fig. 4), with no evident breaks associated with changes in satellite. Final evidence to support our use of satellite data in trend detection is provided in Fig. 1e and Extended Data Fig. 5. These figures show positive trends in MCS frequency only in specific regions in Africa. If there were a series of sensor drifts across instruments and, in the case of GridSat, cross-calibration errors, these would contribute towards positive trends everywhere that MCSs occur.

Rain-gauge data. We used daily rainfall data from 42 sites located between 9.6°N and 15.3°N , 4.8°W and 6.1°E , for the period 1950 to 2015, to analyse changes in the contribution of extreme daily rain to seasonal totals in Fig. 1 (note that the number of sites increases to 44 in Extended Data Fig. 1). We repeated the methodology used in a previous study¹⁷, where ‘extreme daily rain’ is defined as that which exceeds a given threshold (constant over the period, but varying from one gauge to another). This threshold was defined using extreme value theory and corresponds to the expected value that is exceeded twice a year. To quantify JJAS mean rainfall across the larger domain (15°W to 15°E , 11°N to 18°N), we used the CRU 3.23 monthly gridded rainfall data set (available from https://crudata.uea.ac.uk/cru/data/hrg/cru_ts_3.23/). Interannual rainfall in this data set is highly correlated with the frequency of MCSs at a threshold of -40°C for the period 1982–2014 (Table 1).

Precipitable-water data. The global positioning system (GPS) precipitable-water data used here come from four stations in Mali, Burkina Faso and Niger, operated between 2005 and 2011, and processed with GAMIT v10.32 scientific software in high-precision mode³³. The GPS precipitable water is an estimate of the total column water vapour. However, owing to the geometry of the measurement, and given that water vapour is mostly concentrated in the lower troposphere, GPS precipitable water reflects variations in water vapour within a horizontal radius of 20–25 km around the site, and the lowest 4–5 km vertically. For Fig. 3, we computed mean precipitable water every 30 minutes relative to the time of arrival of an MCS at the GPS station (according to Meteosat data). To avoid oversampling, we discarded events when they were separated by less than 6 hours from the previous MCS. For the correlations between precipitable water and MCS intensity, we used the minimum brightness temperature recorded locally. A total of 496 events was detected over the four sites between 1500 UTC and 2100 UTC, and these events were combined to build the composite presented in Fig. 3. The moistening (drying) trend preceding (following) the passage of an MCS in Fig. 3 is qualitatively consistent with measurements in other tropical regions³⁴.

Analysis of atmospheric variables. *In situ* observational data networks are both sparse and temporally heterogeneous in many parts of North Africa, particularly

the Sahara. We therefore examined historic temperature trends with multiple data sets. Trends in JJAS temperatures at 2 m in Fig. 2 and Extended Data Fig. 6 are based on *in situ* observations (surface synoptic observations (SYNOP) data were downloaded from <http://database.amma-international.org>; existing data compilations from Berkeley Earth³⁵, GHCN v3.3.0 (ref. 36) and CRUTEM4.3 (ref. 37) are available from <http://berkeleyearth.org/data/>, <https://www.ncdc.noaa.gov/ghcnm/>, and <http://www.metoffice.gov.uk/hadobs/crutem4/>) and atmospheric reanalyses (from the ERA-Interim³⁸ and MERRA-2 projects, available from <http://www.ecmwf.int/en/research/climate-reanalysis/era-interim> and <https://gmao.gsfc.nasa.gov/reanalysis/MERRA-2/>). We also include trends computed from microwave sounding unit (MSU) lower-tropospheric temperature retrievals from multiple satellites³⁹ (version 5.6 downloaded from <https://ghrc.nsstc.nasa.gov/home>). This retrieval samples temperatures up to about 8 km, but is strongly weighted towards the lowest 3–4 km. As shown previously²², the detailed patterns of warming in North Africa are not always consistent across different reanalyses, or indeed in gridded screen-level temperature data sets. We therefore interpret detailed structure in individual reanalysis trends with caution. For example, there is a pronounced low-level warming across the Sahelian zone of Chad (15° E to 25° E, 10° N to 15° N) in ERA-Interim that is not found in the other data sets.

We performed correlation analysis between atmospheric properties and MCS intensity (as measured by mean temperature of the MCS) on the event timescale, using reanalysis data from ERA-Interim. We identified 99 MCSs that appeared in the Niamey region of Niger (2° E to 3° E, 13° N to 14° N) between the hours of 1500 UTC and 2100 UTC over the period 2004–2016. We chose this location because the local radiosonde station regularly provides data for assimilation within ERA-Interim. Indeed, we found that the region between Niamey and Ouagadougou, Burkina Faso (1.5° W, 12.4° N) provided the best agreement of any Sahelian location in terms of time series of temperatures depicted in the ERA-Interim and MERRA-2 reanalyses. We computed correlations between observed MCS temperature (at time of appearance) with local temperature, wind and humidity variables from the preceding 1200 UTC reanalysis. In Extended Data Fig. 7 we include only those variables that show significant correlations (at the 95% level) with MCS intensity; precipitable water, along with specific humidity and vorticity at 925 hPa, failed this test. We found that more intense MCSs are positively correlated, at both 925 hPa and 700 hPa, with increased temperature, weaker southerly wind, and reduced relative humidity. In addition, more intense MCSs are, on average, preceded by stronger low-level westerlies and mid-level (600 hPa) easterlies. In terms of zonal wind, the correlations are stronger when considering the difference between low- and mid-levels, rather than when considering them individually (Extended Data Fig. 7e).

To link our results to long-term, large-scale trends in the monsoon, we also computed correlations between atmospheric variables (from ERA-Interim) and observed MCS intensity using annual time series. For the atmospheric variables, we computed zonal means between 15° W and 15° E on all available pressure levels, sampled daily at 1200 UTC throughout JJAS. In the case of the meridional wind variance (an indicator of synoptic variability), we first calculated seasonal mean variance for each grid point by using the anomaly from a five-day running mean. For MCS intensity, we used the annual time series of temperatures shown in Extended Data Fig. 4. Extended Data Fig. 8 presents the correlations as a set of meridional cross-sections through the West African monsoon. Because the observed MCS temperature time series used in this analysis is rather linear (with a correlation coefficient of -0.81 when averaged across different times of day), the spatial structure of the correlations with MCS intensity closely resembles that of the trend in the different variables (shown for temperature and wind components in Extended Data Fig. 8g–i). The trend towards more intense MCSs is correlated with rising temperatures throughout the Saharan PBL (up to around 600 hPa north of 20° N), and its southerly extension, the SAL, which overlies the shallower Sahelian PBL. We interpret the correlation patterns of the dynamical variables in terms of this warming: to the south of the enhanced Saharan heat low, the thermal wind response strengthens low-level westerlies and mid-level easterlies (Extended Data Fig. 8b, h); in the north–south direction, the enhanced meridional temperature gradient leads to increased southerly winds (and ‘downgliding’ along isentropic surfaces, which tilt equatorward with height; Extended Data Fig. 8c, i); and in the Northern Sahel and Southern Sahara, increased synoptic variability occurs below 700 hPa, consistent with increased baroclinic instability. Note that we also considered potential impacts of sub-seasonal sampling on our interannual correlations. Specifically, we compared trends in midday sampling of atmospheric variables on all days, with trends computed using only data from days and locations in which MCSs were detected either the following or the previous afternoon or evening. Trends in both pre- and post-event low-level temperatures in the Sahel

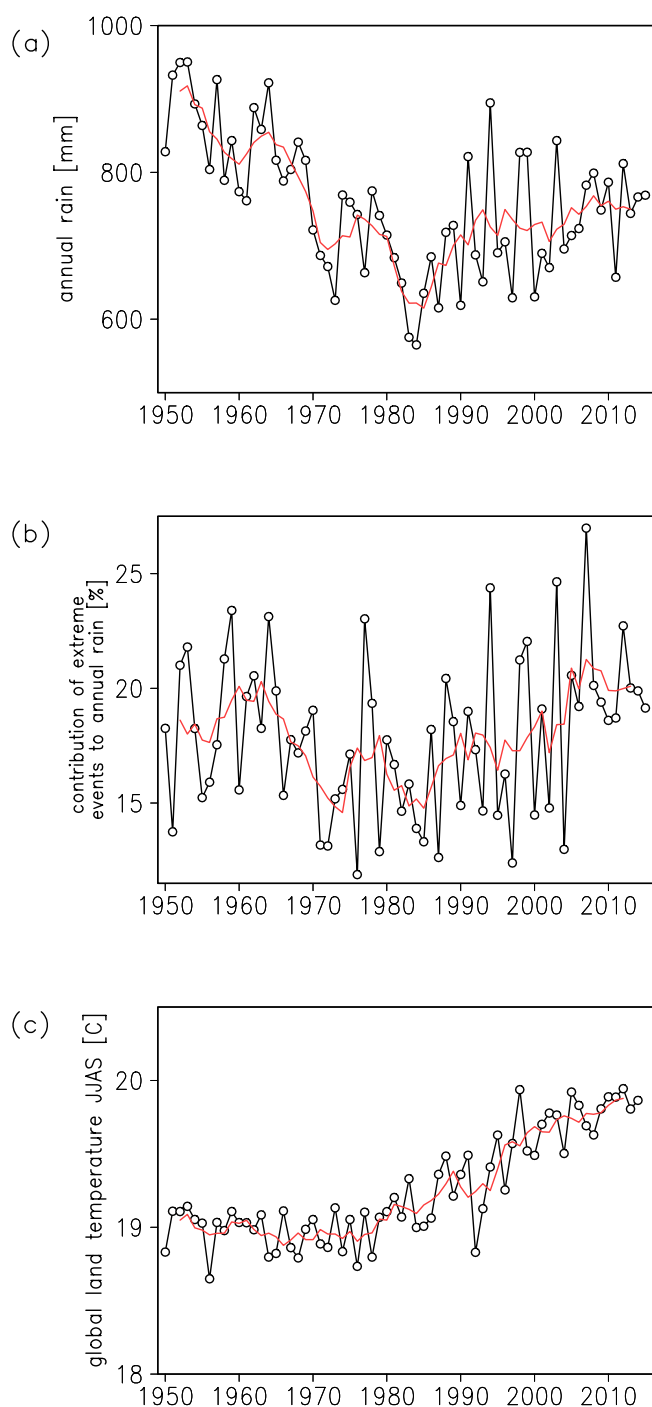
were slightly negative, indicating that intensifying MCSs are not the primary cause of long-term Sahelian cooling. The mean cooling is more likely to be related to the increasing frequency of moderate MCSs, rainfall and cloudiness.

The long-term observational upper-air record in the Sahel is very sparse, both geographically and in terms of pressure levels for which key variables are reported. We examined monthly-mean series from the Integrated Global Radiosonde Archive (IGRA)⁴⁰ (<ftp://ftp.ncdc.noaa.gov/pub/data/igra/>), the Radiosonde Atmospheric Temperature Products for Assessing Climate data set B (RATPAC-B)⁴¹ (<ftp://ftp.ncdc.noaa.gov/pub/data/ratpac/>), and Yale⁴², all of which are based on sounding data but use different correction and adjustment procedures, and from the radiosonde archive maintained by the University of Wyoming (<http://weather.uwyo.edu/upperair/sounding.html>), as well as the monthly-mean gridded products HadAT⁴³ (<http://www.metoffice.gov.uk/hadobs/hadat/>) and Radiosonde Observation Correction Using Reanalyses (RAOBCORE) and Radiosonde Innovation Composite Homogenization (RICH)⁴⁴ (<ftp://srvx7.img.univie.ac.at/>). From these data sets, we were able to confirm the existence of a trend in both warming of the SAL (at 700 hPa) relative to the underlying PBL (at 850 hPa), and increased easterlies at 700 hPa.

To shed light on the role of anthropogenic emissions of greenhouse gases and aerosols, we include diagnostics from the CMIP5 GCM ensemble⁴⁵ (http://cmip-pcmdi.llnl.gov/cmip5/data_portal.html). We used 37 models run under both the historical and the historicalNat scenarios to create Fig. 2d and Extended Data Fig. 6d. Trends were first computed on each model's native grid and then interpolated to a common resolution. The time series in Fig. 2e were based on this same set of models for the historical (1850–2005) and future (2006–2100) scenarios (representative concentration pathways (RCP) 4.5 and 8.5). The ensemble of historical simulations was also used to assess trends in daily rainfall extremes over the period 1976–2005. For each model and grid cell, we computed the 90th centile daily rainfall rate from the months JJAS over the 30 years, and counted the threshold exceedance per year. We found that the ensemble mean trend in the study area was very small compared with our observations—an increase of the order of 1% over 30 years.

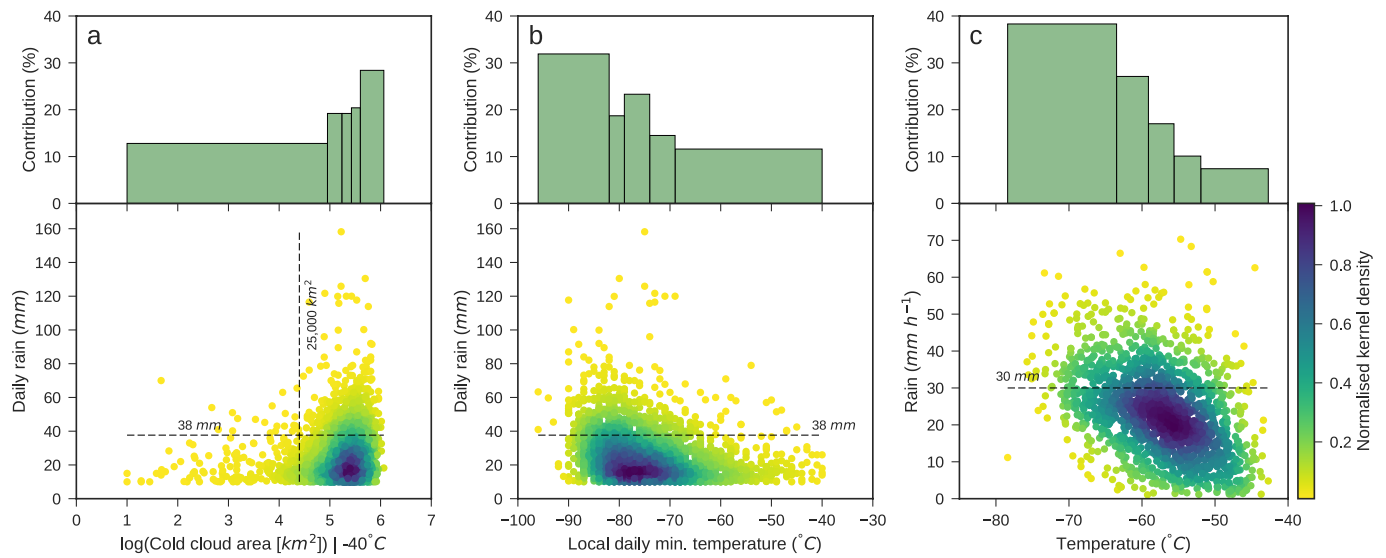
Data availability. The daily station rain-gauge data are subject to third-party restrictions and are not freely available. All of the remaining data used here can be accessed free of charge from the repositories listed above.

- Knapp, K. R. *et al.* Globally gridded satellite observations for climate studies. *Bull. Am. Meteorol. Soc.* **92**, 893–907 (2011).
- Knapp, K. R. Calibration assessment of ISCCP geostationary infrared observations using HIRS. *J. Atmos. Ocean. Technol.* **25**, 183–195 (2008).
- Bock, O. *et al.* West African Monsoon observed with ground-based GPS receivers during African Monsoon Multidisciplinary Analysis (AMMA). *J. Geophys. Res.* **D 113**, D21105 (2008).
- Holloway, C. E. & Neelin, J. D. Temporal relations of column water vapor and tropical precipitation. *J. Atmos. Sci.* **67**, 1091–1105 (2010).
- Rohde, R. *et al.* A new estimate of the average Earth surface land temperature spanning 1753 to 2011. *Geoinfor. Geostat Overview* <http://dx.doi.org/10.4172/2327-4581.1000101> (2013).
- Lawrimore, J. H. *et al.* An overview of the Global Historical Climatology Network monthly mean temperature data set, version 3. *J. Geophys. Res.* **D 116**, D19121 (2011).
- Jones, P. D. *et al.* Hemispheric and large-scale land-surface air temperature variations: an extensive revision and an update to 2010. *J. Geophys. Res.* **D 117**, D05127 (2012).
- Dee, D. P. *et al.* The ERA-Interim reanalysis: configuration and performance of the data assimilation system. *Q. J. R. Meteorol. Soc.* **137**, 553–597 (2011).
- Christy, J. R., Spencer, R. W. & Braswell, W. D. MSU tropospheric temperatures: dataset construction and radiosonde comparisons. *J. Atmos. Ocean. Technol.* **17**, 1153–1170 (2000).
- Durre, I., Vose, R. S. & Wuertz, D. B. Overview of the integrated global radiosonde archive. *J. Clim.* **19**, 53–68 (2006).
- Free, M. *et al.* Radiosonde atmospheric temperature products for assessing climate (RATPAC): a new data set of large-area anomaly time series. *J. Geophys. Res.* **D 110**, D22101 (2005).
- Sherwood, S. C., Meyer, C. L., Allen, R. J. & Titchner, H. A. Robust tropospheric warming revealed by iteratively homogenized radiosonde data. *J. Clim.* **21**, 5336–5352 (2008).
- Thorne, P. W. *et al.* Revisiting radiosonde upper air temperatures from 1958 to 2002. *J. Geophys. Res.* **D 110**, D18105 (2005).
- Haimberger, L., Tavolato, C. & Sperka, S. Toward elimination of the warm bias in historic radiosonde temperature records—some new results from a comprehensive intercomparison of upper-air data. *J. Clim.* **21**, 4587–4606 (2008).
- Taylor, K. E., Stouffer, R. J. & Meehl, G. A. An overview of CMIP5 and the experiment design. *Bull. Am. Meteorol. Soc.* **93**, 485–498 (2011).



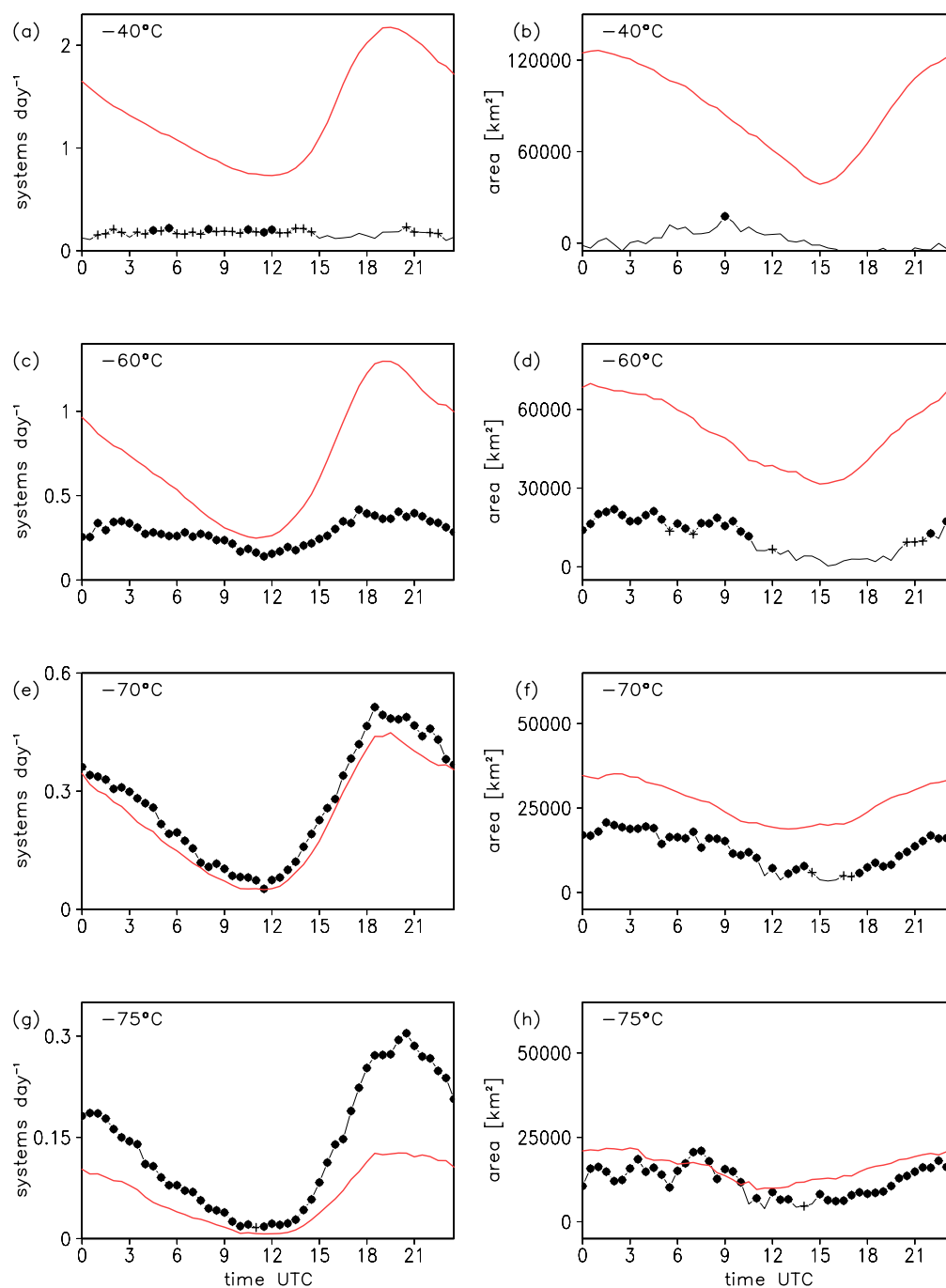
Extended Data Figure 1 | Rainfall and temperature time series

1950–2015. **a**, Annual mean rainfall (in mm), and **b**, contribution of extreme rain events to the annual rainfall total (as a percentage), from the daily rainfall data set in the Central Sahel. **c**, Global land mean temperatures for JJAS from the Climatic Research Unit (CRU) data set (https://crudata.uea.ac.uk/cru/data/hrg/cru_ts_3.23/). Note that data for 2015 were not included in the CRU data. Five-year running means are shown as a red line.



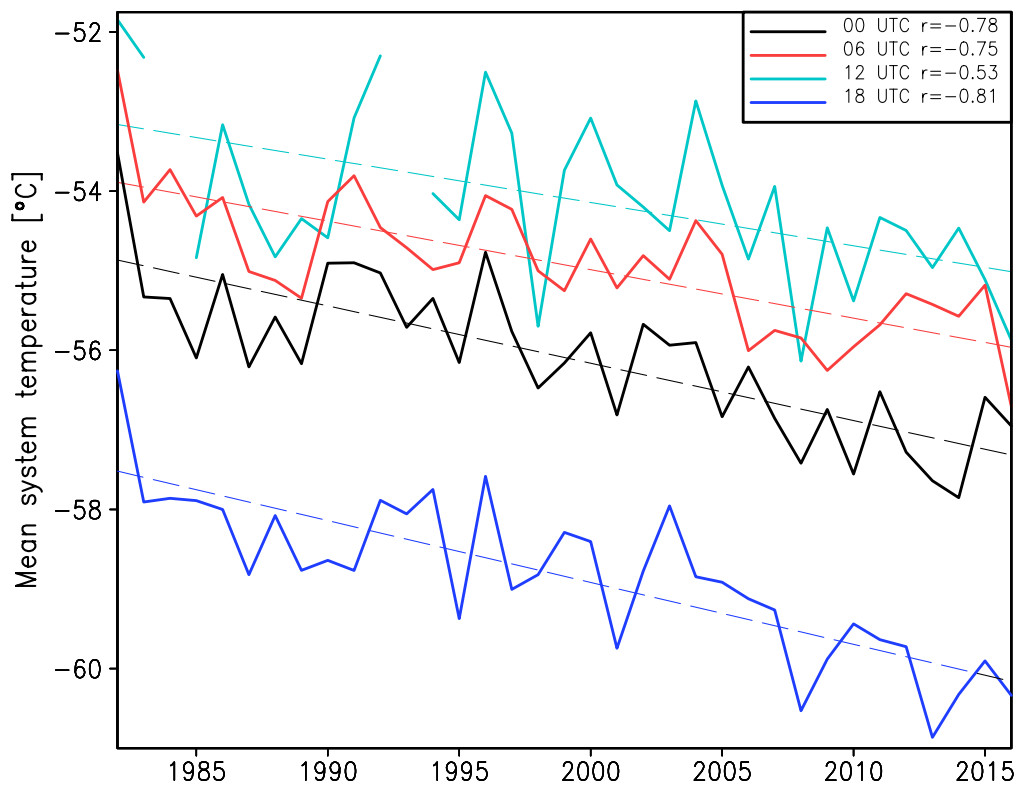
Extended Data Figure 2 | Comparison between observations of extreme rainfall and measures of cold cloud from MSG data. **a, b,** In the bottom graphs, daily rainfall (in mm; values of less than 10 mm are excluded), recorded at 19 Sahelian gauges in 2004–2015, is plotted against the logarithm of the maximum area of contiguous cold cloud (**a**) and the minimum local brightness temperature (in °C) for MCSs greater than 25,000 km² (**b**). **c,** Mean MCS temperature is plotted as a function of the

maximum rainfall rate from TRMM precipitation radar, based on 1,640 coincident overpasses. Each point is shaded according to its normalized kernel density. The bars in the upper plots show the percentage contribution of equally populated quintiles to the total number of extreme events (greater than 38 mm for **a** and **b**; greater than 30 mm per hour for **c**).

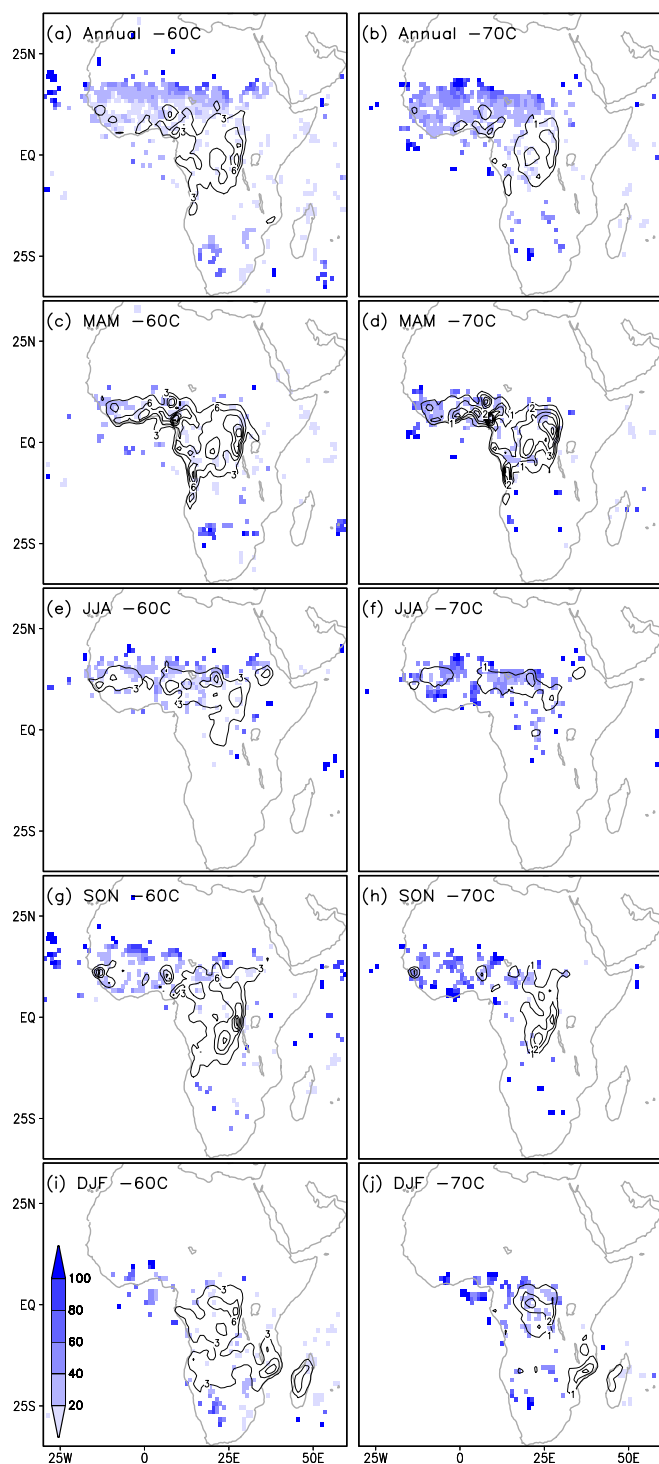


Extended Data Figure 3 | Diurnal cycle of MCS properties. a–h, Diurnal mean MCS frequencies (red line; left panels) and 90th percentile cold-cloud areas (red line; right panels), for temperature thresholds of -40°C (a, b), -60°C (c, d), -70°C (e, f), and -75°C (g, h). Also shown are the trends

(black lines) in these quantities, expressed in terms of the linear regression gradient multiplied by the length of the data set (35 years). Trends that are significant (according to a two-tailed *t*-test) at the 99.5% (or 95%) are denoted by a circle (or a plus sign).

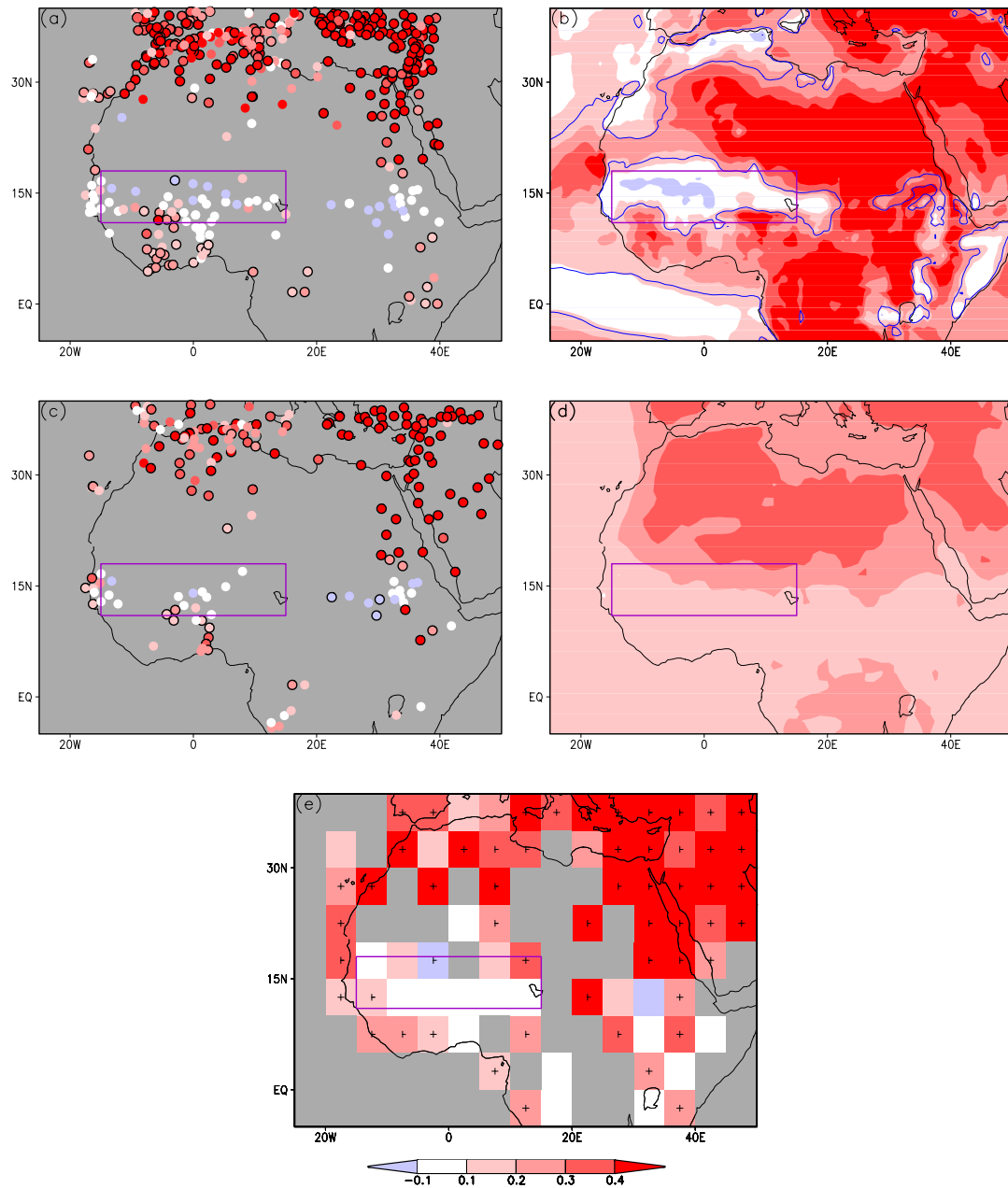


Extended Data Figure 4 | Mean temperature of MCSs identified from GridSat data using a temperature threshold of -40°C . Temperatures (in $^{\circ}\text{C}$) are presented as JJAS averages, sampled at four different times of day. Linear trends are shown as dashed lines, and the values of associated correlation coefficients (r) are quoted.



Extended Data Figure 5 | Trends in MCS cloud cover at 1800 UTC.

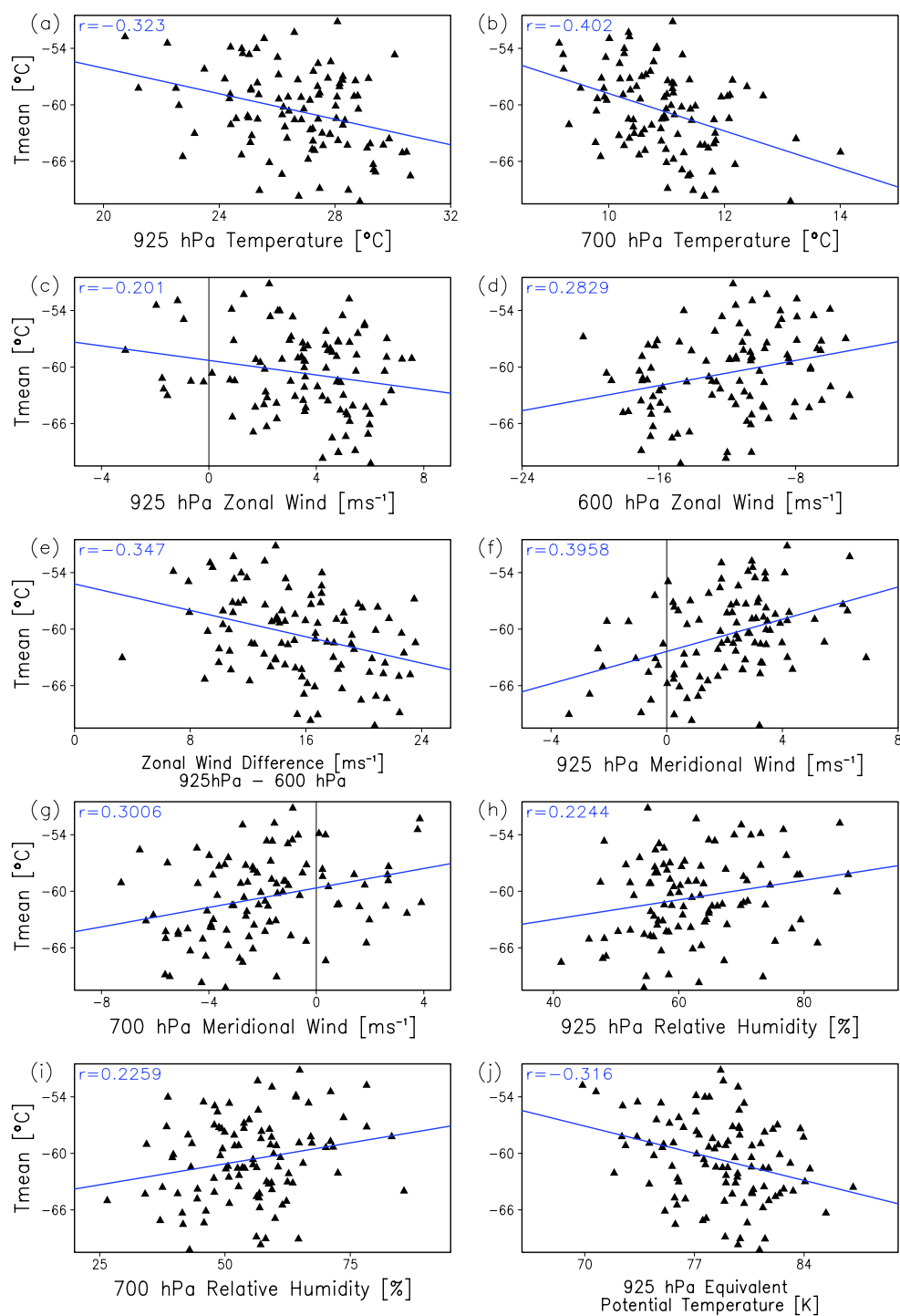
a–j. Shaded pixels denote significant trends in MCS cloud cover ($P < 0.05$) over the full annual cycle (**a, b**), March to May (**c, d**), June to August (**e, f**), September to November (**g, h**), and December to February (**i, j**), using data from 1982–2015. The left-hand column uses a temperature threshold of -60°C ; the threshold for the right-hand column is -70°C . Trends are expressed as the percentage change per decade relative to the long-term mean (shown as contours).



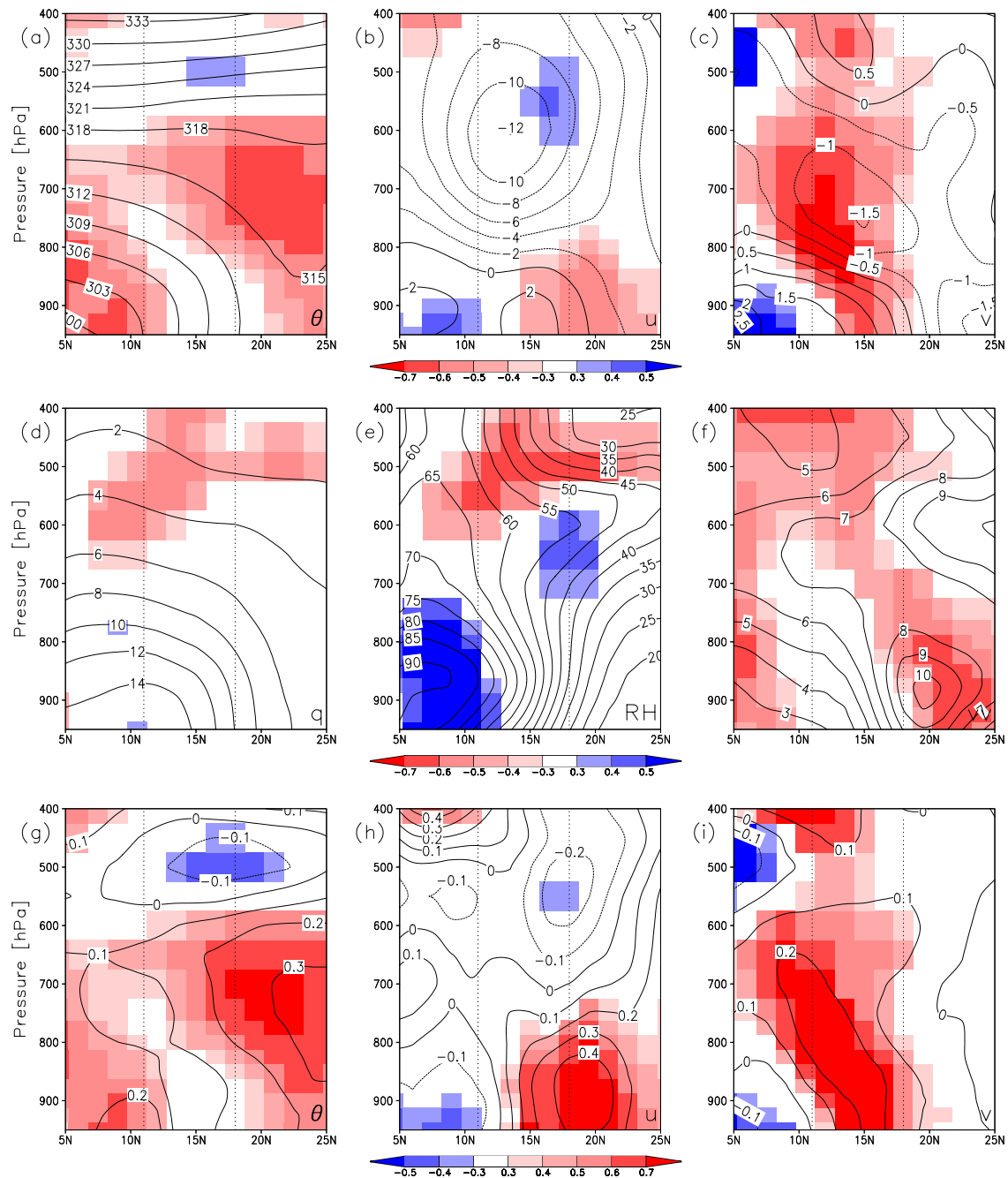
Extended Data Figure 6 | Trends in temperature at 2 metres.

a–e, Temperature trends (°C per decade) from **a**, station data within the Berkeley Earth data set; **b**, MERRA-2 reanalysis; **c**, GHCN station data; **d**, the CMIP5 ensemble mean for ‘all forcings minus natural forcings’; and

e, the gridded station data of CRUTEM4. Trends significant at the 95% level are shown as circles with black edges in panels **a** and **c**; with plus signs in **e**; and enclosed by a blue contour in **b**.



Extended Data Figure 7 | Event-based correlations between pre-MCS atmospheric variables and observed MCS mean temperature on arrival at Niamey. a–j, The pre-MCS variables (x-axes) are from ERA-Interim. All linear regressions are significant at the 99.55% level according to a two-tailed t -test, with the exception of c, h and i, which are significant at the 95% level.



Extended Data Figure 8 | Trends and correlations with MCS intensity of zonal and annual mean variables from ERA-Interim. a–i, Correlation coefficients (shaded where significant at $P < 0.05$) showing the relationship of atmospheric variables with a–f, observed Sahelian MCS (-40°C threshold) mean temperature, and g–i, year. In a–f, contours depict mean values of: a, potential temperature (in K); b, zonal wind (in m s^{-1}); c, meridional wind (in m s^{-1}); d, specific humidity (in g kg^{-1}); e, relative humidity (as a percentage); and f, variance of meridional

wind (in $\text{m}^2 \text{s}^{-2}$). In g–i, the contours show the trends in: g, potential temperature (in K per decade); h, zonal wind (in $\text{m s}^{-1} \text{decade}^{-1}$); and i, meridional wind (in $\text{m s}^{-1} \text{decade}^{-1}$). Dotted lines depict the latitudinal limits of the Sahel. Note that negative correlations with MCS temperature (that is, positive correlations with intensity; a–f), and positive correlations with time (g–i) are shaded red for ease of comparison. The colour bars show correlation coefficients.